Magnetic Breakdown and Topology in the Kagome Superconductor CsV_3Sb_5 under High Magnetic Field

Ramakanta Chapai[1,*] Maxime Leroux,[2] Vincent Oliviero,[2] David Vignolles,[2]
Nicolas Bruyant,[2] M. P. Smylie,[1,3] D. Y. Chung,[1] M. G. Kanatzidis,[1,4] W.-K. Kwok,[1]
J. F. Mitchell,[1] and Ulrich Welp[1,†]

[1]*Materials Science Division, Argonne National Laboratory, Lemont, Illinois 60439, USA*
[2]*LNCMI-EMFL, CNRS UPR3228, Université Grenoble Alpes, Université de Toulouse,
Université de Toulouse 3, INSA-T, Grenoble and Toulouse, France*
[3]*Department of Physics and Astronomy, Hofstra University, Hempstead, New York 11549, USA*
[4]*Department of Chemistry, Northwestern University, Evanston, Illinois 60201, USA*

The recently discovered layered kagome metals of composition AV_3Sb_5 (A = K, Rb, Cs) exhibit a complex interplay among superconductivity, charge density wave order, topologically nontrivial electronic band structure and geometrical frustration. Here, we probe the electronic band structure underlying these exotic correlated electronic states in CsV_3Sb_5 with quantum oscillation measurements in pulsed fields up to 86 T. The high-field data reveal a sequence of magnetic breakdown orbits that allows the construction of a model for the folded Fermi surface of CsV_3Sb_5. The dominant features are large triangular Fermi surface sheets that cover almost half the folded Brillouin zone. These sheets have not yet been detected in angle resolved photoemission spectroscopy and display pronounced nesting. The Berry phases of the electron orbits have been deduced from Landau level fan diagrams near the quantum limit without the need for extrapolations, thereby unambiguously establishing the nontrivial topological character of several electron bands in this kagome lattice superconductor.

The interplay of superconductivity, charge density wave (CDW) order, and nontrivial topology of the electronic band structure in the metallic kagome lattice compounds AV_3Sb_5 (A = K, Rb, Cs) has generated substantial interest in the effects arising from van Hove singularities, Dirac crossings, electronic correlations, and geometrical frustration [1–7]. For instance, an unusual relationship between the CDW and superconductivity (SC) has been reported via pressure and doping studies: mechanical or chemical pressure induces a double-dome shaped superconducting phase diagram in CsV_3Sb_5 [8–13]. If the SC and CDW states compete for the same electrons at the Fermi surface [14,15], suppressing CDW order should enhance T_c, suggesting an unconventional SC state in CsV_3Sb_5. The CDW order in CsV_3Sb_5 is itself fascinating due to the presence of chiral charge order and time-reversal symmetry breaking without local magnetic moments [16–21]. This state is believed to give rise to a large anomalous Hall effect [4,5,22]. The transition into the CDW state is accompanied by an in-plane unit cell doubling [3] and the concomitant folding of the Fermi surface and appearance of CDW-induced gaps, which mostly affect bands derived from vanadium d orbitals. Furthermore, in the out-of-plane direction, doubling [23,24] or quadrupling [3] of the unit cell have been reported.

Detailed knowledge of the reconstructed electronic band structure is prerequisite for understanding the interplay between different charge orders, flux phases, and possible unconventional superconductivity in the AV_3Sb_5 family. While angle resolved photoemission spectroscopy (ARPES) has been invaluable in exploring the electronic structure, effects due to matrix elements have largely precluded the visualization of the folded band structure [25–27]. In contrast, quantum oscillations (QOs) are a direct manifestation of the actual Fermi surface revealing information on the quasiparticle effective masses, their lifetimes, and their topological state. Here, we report on quantum oscillations observed in high-quality single crystal CsV_3Sb_5 in pulsed magnetic fields up to 86 T. Twenty-five distinct frequencies ranging from 20 to 9930 T have been identified, with most of the high-frequency bands as new findings. In particular, the high-field data yield a sequence of magnetic breakdown orbits that allow us to construct a model for the folded Fermi surface. The dominant features are large triangular Fermi surface sheets that cover almost half of the folded Brillouin zone (BZ) that have not been seen via ARPES [6,26]. These sheets display pronounced nesting in the folded Fermi surface. Using the Lifshitz-Kosevich (LK) formalism [28] we determine effective masses ranging from $0.17m_0$ to $2.02m_0$ (m_0 is the free-electron mass). The Berry phases of the electron orbits are deduced from Landau level (LL) fan diagrams. Because of the very high magnetic field, we can evaluate the phase of quantum oscillations near the quantum
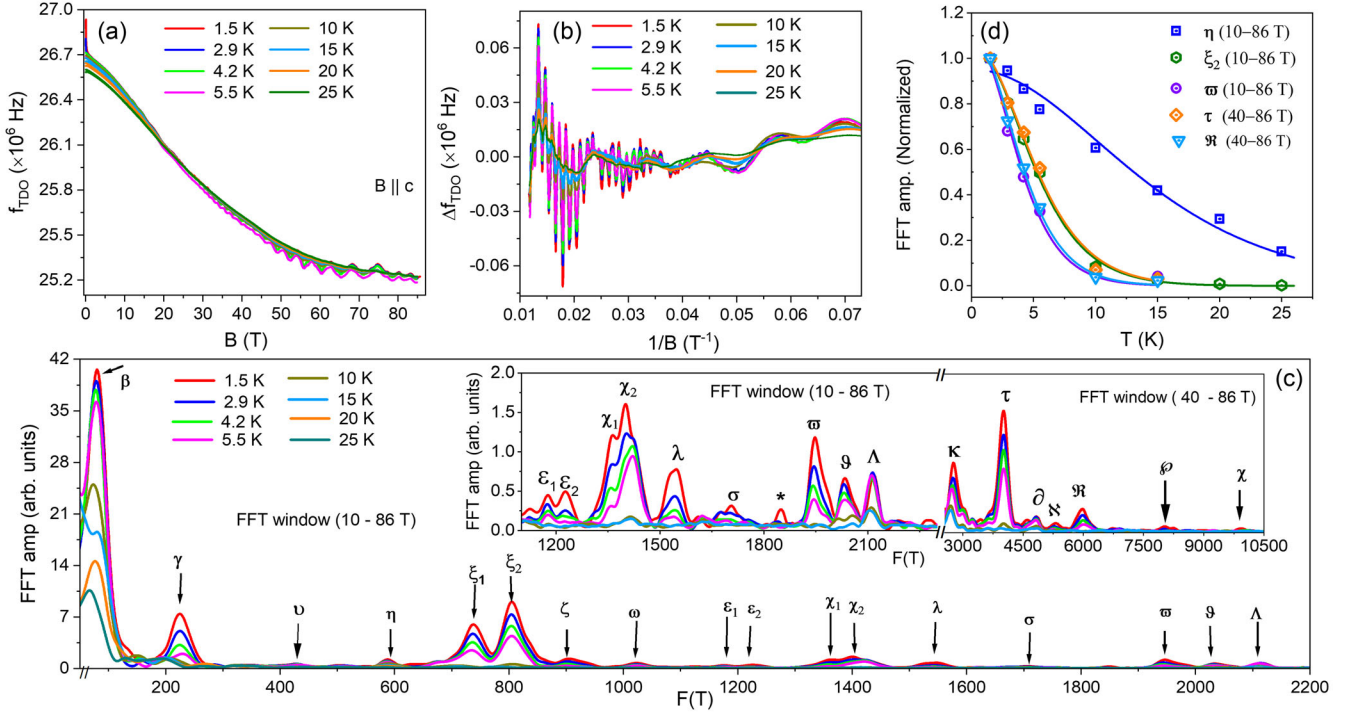
FIG. 1. (a) Field dependence of the TDO frequency (f_{TDO}) of CsV$_3$Sb$_5$ at various temperatures. (b) SdH oscillations visible in Δf_{TDO} after the subtraction of the nonoscillatory part, plotted as a function of $1/B$. (c) FFT spectrum of data presented in frame (b). Inset: the FFT spectra displaying high frequencies. (d) Temperature dependence of the FFT amplitudes for indicated bands. Solid lines are fits with thermal damping term of Eq. (S1) [32]. The numbers in the parenthesis in frame (c) and (d) denote the field range used for the FFT analysis.

limit, thereby unambiguously revealing the nontrivial topological character of the β ($F_\beta = 79$ T), the ξ_1 ($F_{\xi 1} = 736$ T), and the ξ_2 ($F_{\xi 2} = 804$ T) bands. The latter two bands are derived from Dirac crossings at the K and H points in the BZ, respectively, which our results place at 290 and 350 meV below the Fermi level (E_F) while the former is derived from a crossing at the A point (corresponding to the L point in the unfolded BZ) at 107 meV below the E_F.

Quantum oscillation measurements using the tunnel diode oscillator (TDO) technique [29–31] were performed at the pulsed-field facility in the Toulouse National Intense Magnetic Field Laboratory (LNCMI-T) CNRS (see Supplemental Material [32] for more details). Figure 1(a) displays the field dependence of the TDO frequency (f_{TDO}) of single crystalline CsV$_3$Sb$_5$ measured in magnetic fields applied parallel to the c axis.

The quantum oscillation observed as the oscillatory part of the TDO frequency, Δf_{TDO}, obtained after subtracting a smooth background [32] is plotted as a function of inverse field ($1/B$) in Fig. 1(b). A complex spectrum with 25 distinct oscillation frequencies emerges from the fast Fourier transformation (FFT) analysis of the data with frequencies ranging from 20 to 9930 T as shown in Fig. 1(c). The very high frequencies exceeding 2700 T are new findings reported here. Table S1 [32] summarizes all the frequencies shown in Fig. 1(c).

As the oscillatory TDO signal is a measure of the temperature and field dependence of the conductivity, we use the LK formalism for the analysis of Shubnikov–de Haas (SdH) oscillations [28,32–34]. Figure 1(d) displays the temperature dependence of the FFT amplitudes for several bands. From fits of the observed temperature dependences to the thermal damping factor [Eq. (S1) [32]] we obtain cyclotron effective masses $m_\eta^* = 0.19m_0$, $m_{\xi 2}^* = 0.52m_0$, $m_\varpi^* = 0.69m_0$, $m_\tau^* = 1.57m_0$, and $m_\Re^* = 2.02m_0$. Data for additional bands are shown in Fig. S3 and in Table S1 of the Supplemental Material [32]. In addition to bands with very light masses, already seen in previous studies [3,35–39], we observe "heavier" bands with effective masses approaching 2. Such heavier bands are expected as van Hove singularities are contributing to the electronic structure near the Fermi energy [6,40].

The 1st BZ of a hexagonal lattice with lattice constant a has an area of $8\pi^2/(\sqrt{3}a^2)$ which, in the case of CsV$_3$Sb$_5$, is ~ 1.55 Å^{-2} corresponding to a quantum oscillation frequency of 16.24 kT. In the CDW state, the BZ is folded to one-quarter of its pristine size, that is, a frequency of about 4060 T. This implies that all the high frequencies observed in Fig. 1(c) either represent harmonics of lower frequency orbits or are caused by magnetic breakdown or quantum interference [28]. Magnetic breakdown [28,41–44] can arise when two extremal orbits on different sheets of the Fermi surface are so close (in k

space) that an electron (hole) can tunnel from one orbit to the other and continue its trajectory, thereby inducing sum and difference frequencies in the spectrum. Their collective behavior can be described in a model of coupled networks of semiclassical electron trajectories yielding a relation for the oscillatory energy that is similar to the LK formula albeit with an additional damping factor characterizing the tunneling events [41,45]. The prevalence of magnetic breakdown is indicated by Dingle plots [28,46] displaying a clear nonmonotonic behavior (Fig. S4 [32]).

The spectrum in Fig. 1(c) reveals a series of high-frequency orbits, $F_\varpi = 1943$, $F_\tau = 4025$, $F_\mathcal{R} = 5996$, $F_\mathcal{L} = 8014$, and $F_\mathcal{X} = 9930$ T that are approximately equally spaced at ~ 2000 T. Such a sequence could arise due to higher harmonics of the ϖ orbit, magnetic breakdown orbits or quantum interference involving multiple copies of the ϖ orbit. Higher harmonics have effective masses that are enhanced by the harmonic order over that of the fundamental, whereas the effective mass of breakdown orbits (between like carriers) and quantum interferences equals the sum and difference of the involved masses, respectively [44,47,48]. Experimentally, we find that the effective masses of the high-frequency orbits F_ϖ, F_τ, and $F_\mathcal{R}$ scale approximately as multiples (see Table S1 [32] and above) thus ruling quantum interference out as the mechanism of high-frequency orbits. Our data indicate that the successive frequencies correspond to the addition of a unit to the orbit that is robust in very high fields and that occupies close to half the folded BZ. While the details of the reconstructed Fermi surface are currently not well established [37], the high-field behavior yields additional constraints and allows construction of a model that captures the observed behavior, as shown in Fig. 2 (also see Fig. S5 [32]). The schematic [Fig. 2(a)] suggests that the triangular orbit (shown in magenta) centered on the H point and spanned by three A points labeled 1, 2, 4 is the most likely building block for the high-frequency orbits [see Fig. 2(b)], and we identify it with F_ϖ.

The experimental frequencies are systematically larger than expected for a harmonic, $n \times F_\varpi$. The τ orbit has a frequency of 4025 T which is very close to the full folded BZ, labeled 1, 2, 3, 4 in Fig. 2(a), see also Fig. S6(a) in Ref. [32]. This orbit can arise through magnetic breakdown near two A points (2,4) as depicted in Fig. 2(a), implying that this orbit has an area of two triangular ϖ-orbits plus the area of the narrow lamella centered on L between two close magenta sheets, the area of which we estimate to be ~ 100 T, even though the details of the Fermi surface (FS) near the L point are uncertain. The 120-degree turns in the τ orbit at locations 2 and 4 trace the orbit of the pristine FS and are therefore natural to arise during breakdown [Fig. 2(c)]. Following this scheme, we identify the $\mathcal{R}$ orbit (5996 T) with three triangular plaquettes [Fig. S6(b)], the $\mathcal{L}$ orbit (8014 T) with four and a line at $F_\mathcal{X} = 9930$ T with five triangular plaquettes. Thus, our high-field observations
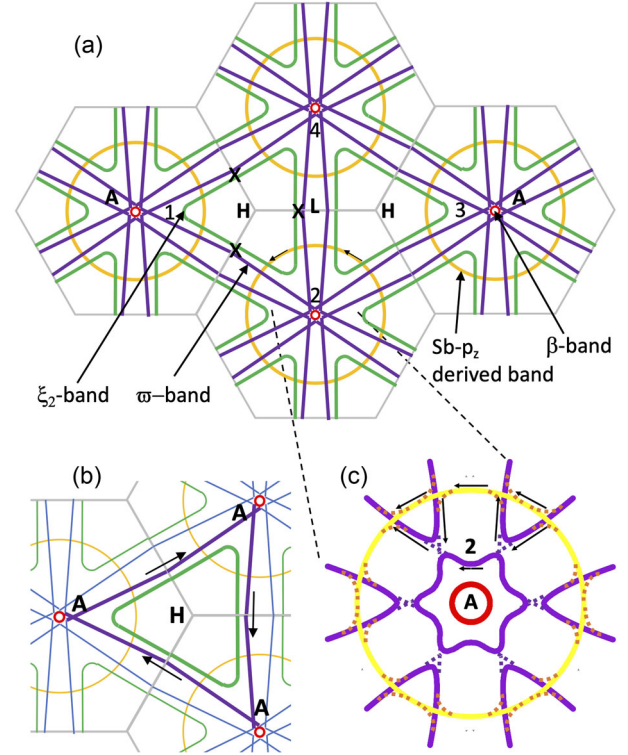

FIG. 2. (a) Schematic of the 2×2 folded Fermi surface of CsV$_3$Sb$_5$ for $k_z = \pm\pi/c$ in repeated zones. The crosses indicate likely breakdown junctions between the ξ_2 and ϖ orbits. (b) Enlarged schematic highlighting the ξ_2 and ϖ orbits. (c) Enlarged schematic showing details around the A point as indicated by the dashed lines. For clarity, ξ_2 orbits are not included, and the yellow sheet is drawn at reduced size as compared to (a). The locations of breakdown are indicated as dashed lines. The arrows indicate the semiclassical trajectories of the carriers.

reveal a remarkable network of reconstructed Fermi surface sheets that displays a high degree of nesting. As shown in Fig. 2(a), the Fermi velocity is essentially unidirectional over extended sections of the Fermi surface, which is expected to yield characteristic signatures in magneto-transport [49] and thermodynamic properties such as the temperature dependence of the upper critical field or of the penetration depth. While DFT calculations indicate that the ϖ band persists at the H, K, and L points, near the M point it is gapped [6,7,36]. Detailed angular dependent studies in high fields will be required to establish the three-dimensional structure of the reconstructed Fermi surface.

Based on recent quantum oscillation measurements and band-structure calculations [36], we identify the triangular sheet centered on the H point [presented in green, Fig. 2(b)] with the ξ_2 orbit having a frequency of 804 T. Accordingly, ξ_1 (736 T) represents the corresponding triangular sheet centered on the K point ($k_z = 0$). A carrier can tunnel from the ϖ orbit to the ξ_2 orbit at the point of smallest separation on the LH line marked by crosses in Fig. 2(a), complete the ξ_2 orbit, tunnel back to ϖ at the same point, and complete

the ϖ orbit resulting in a sum frequency of $F_\varpi + F_{\xi2}$ of 2747 T which is close to the observed frequency of $F_\kappa = 2753$ T. Furthermore, the measured effective mass of $1.13m_0$ is close to the expected value of $1.21m_0$. Similarly, the ∂ orbit with a measured frequency of $F_\partial = 4827$ T results from the same breakdown mechanism between the τ and the ξ_2 orbits with an expected frequency of 4829 T.

In addition to a complete ξ_2 orbit, the carrier can tunnel back to the ϖ orbit at the next point of proximity after completing $1/3$ of the ξ_2 orbit or at the following point of close proximity after completing two-thirds of the ξ_2 orbit. These trajectories will generate quantum oscillation frequencies of $2/3F_\varpi + 1/3F_{\xi2} = 1563$ and of $1/3F_\varpi + 2/3F_{\xi2} = 1183$ T, respectively, in very good agreement with the observed frequencies $F_\lambda = 1550$ and $F_{\varepsilon1} = 1170$ T. The corresponding measured effective masses of $0.86m_0$ and $0.54m_0$ appear in reasonable agreement with the expected values of $0.66m_0$ and $0.57m_0$. Near the L point of the reconstructed BZ, sections of the triangular-shaped ξ_2 orbits are almost parallel, resulting in a pronounced nesting with a nesting vector amounting to approximately 20% of the CDW vector [see Fig. S5(c) [32]]. The $F_\beta \sim 79$ T frequency, accompanied by a small effective mass of $0.17m_0$ ([32]) has been observed consistently in all previous works [3,4,35–39]. These parameters are close to those reported for a small prolate ellipsoid shaped FS near the L point in the pristine BZ [36] which, upon reconstruction, appears at the A point of the folded zone (small red circle in Fig. 2). The star-shaped orbit near the zone center arises from intersecting and gapping of the magenta sheets, see Fig. 2(c). We identify this orbit with F_γ motivated by its small size and the fact that it has the same effective mass as the ϖ orbit. This orbit is an electron orbit. Our data did not enable the identification of the circular electron orbits centered on $\Gamma - A$ and derived from Sb p_z states (shown in yellow in Fig. 2). A likely cause is the large number of breakdown junctions, 24, encountered on these orbits making them difficult to observe in quantum oscillations. Furthermore, some bands in Fig. 1(c) remain unassigned, most notably ϑ, Λ, and the χ_1-χ_2 pair which has the same splitting, 68 T, as ξ_1 and ξ_2. Possibly, these frequencies are associated with the 3D-structure of the Fermi surface, orbits in the $k_z = 0$ plane, and c-axis reconstruction [50]. The complete indexing and the explanation of the apparent grouping in the observed oscillations frequencies requires a systematic determination of the 3D Fermi surface of CsV_3Sb_5.

Following the LK formalism, the phase of the oscillatory conductivity at a given frequency reveals the Berry phase, that is, the topological state of the orbit in question. The oscillatory component of Δf_{TDO} for a given frequency is isolated via a filtering process [51]. Figure 3(a) shows Δf_{TDO} versus B^{-1} for the β band isolated by using a band-pass filter (60–100 T). The Landau fan diagram is
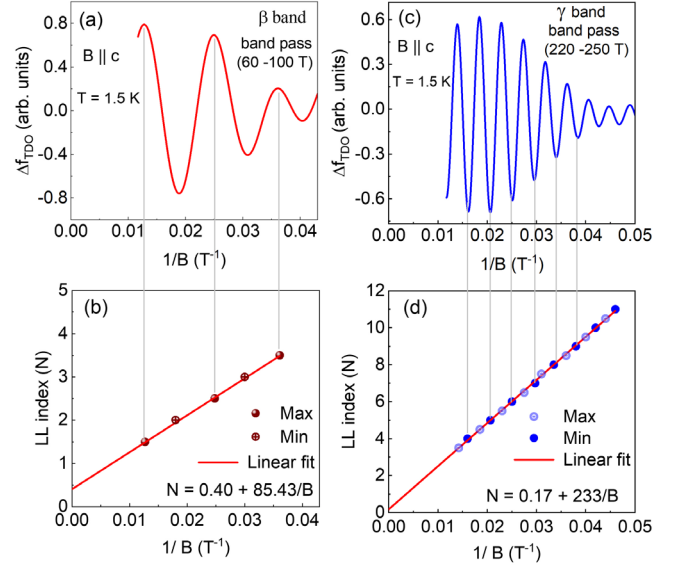

FIG. 3. (a) Δf_{TDO} of the β band plotted as a function of inverse magnetic field (B^{-1}). (b) Landau fan diagram constructed from the SdH oscillations in frame (a). (c),(d) Similar data for the γ band. The solid lines in frames (b) and (d) are linear fits of the data.

constructed by assigning the SdH oscillation minima to N, the LL index and maxima to $N + 1/2$ [33]. As shown in Fig. 3(b), $N(B^{-1})$ can be fitted as $N = 0.40 + F/B$ yielding a frequency of $F_\beta = 85.43$ T, in good agreement with that obtained from the FFT spectra [Fig. 1(c)]. This implies that the filtering process to isolate the β orbit preserves the original signal. The intercept of this linear equation gives the Berry phase as $(\Phi_B^\beta/2\pi) + \delta = 0.40$. This band has previously been identified as a prolate electron ellipsoid [36], thus $\delta = -1/8$ [52]. With this consideration, $\Phi_B^\beta \sim \pi$, a nontrivial Berry phase [53]. As the charge carriers reach the first LL (near the quantum limit) at 86 T for the β band, we can determine the intercept in the LL plot without extrapolation from high LL indices thus unambiguously establishing the nontrivial topology of the β band. The nontrivial Berry phase accompanied by a small effective mass confirms the underlying nontrivial topology predicted by DFT calculations [2,3,36].

Similarly, the LL fan diagrams constructed for the γ orbit [Figs. 1(c) and 1(d)] and η-orbit [Fig. S7(a) [32]] yield intercepts of ~ 0.2 and ~ 0, respectively. Thus, these two orbits have trivial topology. Even though very high frequency bands (e.g., τ and $\mathcal{R}$) can be isolated with filtering hence enabling the construction of the LL fan diagrams, determining the Berry phase for those bands requires an extrapolation from high LL indices [Fig. S7(g–h) [32]]. In addition, magnetic breakdown can induce additional phase shifts [28,41–43] inducing uncertainty in the determination of the Berry phase.

Nevertheless, as demonstrated in Fig. S7(d)–7(h), the LL fan diagrams for the ω, κ, τ, and $\mathcal{R}$ orbits display the intercepts of ~ 0, ~ 0.5, ~ 0, and 0.5, respectively, and the linear fits yield frequencies in good agreement with the spectral analysis. Furthermore, we verified that the extrapolations do not depend on the field range (Fig. S7) demonstrating that there are no field-induced changes in the electron-orbits at high fields. For the ξ_1 and ξ_2 bands, we obtain Berry phases of $\sim 1.32\pi$ and 1.14π [shown in Figs. S7(b),7(c) [32]] identifying these bands as nontrivial, consistent with them being derived from Dirac crossings at the K and H points, respectively. Using the linear relativistic Dirac dispersion, given as $E - E_D = \hbar v_D k$, and an area of the orbit assumed to be circular, we obtain the location of the Dirac crossing, E_F-E_D, and the Dirac velocity, v_D, in terms of measured quantities as $v_D = \sqrt{2e\hbar F}/m^*$ and E_F-$E_D = 2e\hbar F/m^*$, yielding $v \sim 2.9 \times 10^5$ and 3.5×10^5 m/s, and E_F-$E_D \sim 287$ and 353 meV for the ξ_1 and ξ_2 bands, respectively. A similar analysis yields $E_F - E_D \sim 107$ meV for the β band. These estimates for the location of the Dirac crossings are in good agreement with band structure calculations and ARPES results [6,7,36,54,55].

In summary, we discovered sequences of high field breakdown orbits on the reconstructed Fermi surface of CsV_3Sb_5 in pulsed magnetic fields up to 86 T. These results enable the construction of a consistent model for the folded Fermi surface. The dominant features are large triangular Fermi surface sheets that cover almost half of the folded Brillouin zone and are absent in ARPES measurements. A series of QO frequencies can be understood as arising from breakdown orbits encompassing multiples of the triangular sheets. Using the LK formalism, we determined effective masses ranging from $0.17m_0$ to $2.02m_0$, and from LL fan diagrams, deduced the Berry phases of the electron orbits. The very high magnetic field enabled us to evaluate the phase of quantum oscillations near the quantum limit without the need for extrapolations, thereby unambiguously revealing the nontrivial topological character of the β ($F_\beta = 79$ T) band, and of the ξ_1 ($F_{\xi_1} = 736$ T) and ξ_2 ($F_{\xi_2} = 804$ T) bands. The latter two bands are derived from Dirac crossings at the K and H points, respectively. A reconstructed Fermi surface containing extended almost flat sections should yield characteristic signatures in magnetotransport and thermodynamic properties such as the temperature dependence of the upper critical field or of the penetration depth.

*rchapai@anl.gov
†welp@anl.gov

[1] B. R. Ortiz, L. C. Gomes, J. R. Morey, M. Winiarski, M. Bordelon *et al.*, New kagome prototype materials: Discovery of KV_3Sb_5, RbV_3Sb_5, and CsV_3Sb_5, Phys. Rev. Mater. **3**, 094407 (2019).

[2] B. R. Ortiz, S. M. L. Teicher, Y. Hu, J. L. Zuo, P. M. Sarte *et al.*, CsV_3Sb_5: A Z_2 Topological Kagome Metal with a Superconducting Ground State, Phys. Rev. Lett. **125**, 247002 (2020).

[3] B. R. Ortiz, S. M. L. Teicher, L. Kautzsch, P. M. Sarte, N. Ratcliffe, J. Harter, J. P. C. Ruff, R. Seshadri, and S. D. Wilson, Fermi Surface Mapping and the Nature of Charge-Density-Wave Order in the Kagome Superconductor CsV_3Sb_5, Phys. Rev. X **11**, 041030 (2021).

[4] F. H. Yu, T. Wu, Z. Y. Wang, B. Lei, W. Z. Zhuo, J. J. Ying, and X. H. Chen, Concurrence of anomalous Hall effect and charge density wave in a superconducting topological kagome metal, Phys. Rev. B **104**, L041103 (2021).

[5] S.-Y. Yang, Y. Wang, B. R. Ortiz, D. Liu, J. Gayles *et al.*, Giant, unconventional anomalous Hall effect in the metallic frustrated magnet candidate, KV_3Sb_5, Sci. Adv. **6**, eabb6003 (2020).

[6] M. Kang, S. Fang, J.-K. Kim, B. R. Ortiz, S. H. Ryu *et al.*, Twofold van Hove singularity and origin of charge order in topological kagome superconductor CsV_3Sb_5, Nat. Phys. **18**, 301 (2022).

[7] H. Tan, Y. Liu, Z. Wang, and B. Yan, Charge Density Waves and Electronic Properties of Superconducting Kagome Metals, Phys. Rev. Lett. **127**, 046401 (2021).

[8] F. H. Yu, D. H. Ma, W. Z. Zhuo, S. Q. Liu, X. K. Wen, B. Lei, J. J. Ying, and X. H. Chen, Unusual competition of superconductivity and charge-density-wave state in a compressed topological kagome metal, Nat. Commun. **12**, 3645 (2021).

[9] Z. Y. Zhang, Z. Chen, Y. Zhou, Y. F. Yuan, S. Y. Wang, J. Wang, H. Yang, C. An, L. Zhang, X. Zhu, Y. Zhou, X. Chen, J. Zhou, and Z. Yang, Pressure-induced reemergence of superconductivity in the topological kagome metal CsV_3Sb_5, Phys. Rev. B **103**, 224513 (2021).

[10] K. Y. Chen, N. N. Wang, Q. W. Yin, Y. H. Gu, K. Jiang *et al.*, Double Superconducting Dome and Triple Enhancement of T_c in the Kagome Superconductor CsV_3Sb_5 under High Pressure, Phys. Rev. Lett. **126**, 247001 (2021).

[11] H. Yang, Y. Zhang, Z. Huang, Z. Zhao, J. Shi *et al.*, Titanium doped Kagome superconductor $CsV_{3-x}Ti_xSb_5$ and two distinct phases in strong coupling kagome superconductors, Sci. Bull. **67**, 2176 (2022).

[12] Y. M. Oey, B. R. Ortiz, F. Kaboudvand, J. Frassineti, E. Garcia, R. Cong, S. Sanna, V. F. Mitrović, R. Seshadri, and S. D. Wilson, Fermi level tuning and double-dome superconductivity in the kagome metals $CsV_3Sb_{5-x}Sn_x$, Phys. Rev. Mater. **6**, L041801 (2022).

[13] L. Kautzsch, Y. M. Oey, H. Li, Z. Ren, B. R. Ortiz *et al.*, Incommensurate charge-stripe correlations in the kagome superconductor $CsV_3Sb_{5-x}Sn_x$, arXiv:2207.10608.

[14] M. Leroux, V. Mishra, J. P. C. Ruff, H. Claus, M. P. Smylie *et al.*, Disorder raises the critical temperature of a cuprate superconductor, Proc. Natl. Acad. Sci. U.S.A. **116**, 10691 (2019).

[15] M. Leroux, V. Mishra, C. Opagiste, P. Rodiere, A. Kayani, W.-K. Kwok, and U. Welp, Charge density wave and superconductivity competition in $Lu_5Ir_4Si_{10}$: A proton irradiation study, Phys. Rev. B **102**, 094519 (2020).

[16] R. Khasanov, D. Das, R. Gupta, C. Mielke, M. Elender et al., Time-reversal symmetry broken by charge order in CsV_3Sb_5, Phys. Rev. Res. **4**, 023244 (2022).

[17] C. Mielke III, D. Das, J. X. Yin, H. Liu, R. Gupta et al., Time-reversal symmetry-breaking charge order in a kagome superconductor, Nature (London) **602**, 245 (2022).

[18] L. Yu, C. Wang, Y. Zhang, M. Sander, S. Ni et al., Evidence of a hidden flux phase in the topological kagome metal CsV_3Sb_5, arXiv:2107.10714.

[19] Z. Wang, Y.-X. Jiang, J.-X. Yin, Y. Li, G.-Y. Wang et al., Electronic nature of chiral charge order in the Kagome superconductor CsV_3Sb_5, Phys. Rev. B **104**, 075148 (2021).

[20] N. Shumiya, M. S. Hossain, J.-X. Yin, Y.-X. Jiang, B. R. Ortiz et al., Intrinsic nature of chiral charge order in the kagome superconductor RbV_3Sb_5, Phys. Rev. B **104**, 035131 (2021).

[21] H. Zhao, H. Li, B. R. Ortiz, S. M. L. Teicher, T. Park, M. Ye, Z. Wang, L. Balents, S. D. Wilson, and I. Zeljkovic, Cascade of correlated electron state in the kagome superconductor CsV_3Sb_5, Nature (London) **599**, 216 (2021).

[22] G. Zheng, C. Tan, Z. Chen, M. Wang, X. Zhu et al., Electrically controlled superconductor -to-failed insulator transition and giant anomalous Hall effect in kagome metal CsV_3Sb_5 nano flakes, Nat. Commun. **14**, 678 (2023).

[23] Z. Liang, X. Hou, F. Zhang, W. Ma, P. Wu et al., Three-Dimensional Charge Density Wave and Surface-Dependent Vortex-Core States in a Kagome Superconductor CsV_3Sb_5, Phys. Rev. X **11**, 031026 (2021).

[24] H. Li, T. T. Zhang, T. Yilmaz, Y. Y. Pai, C. E. Marvinney, A. Said, Q. W. Yin, C. S. Gong, Z. J. Tu, E. Vescovo, C. S. Nelson, R. G. Moore, S. Murakami, H. C. Lei, H. N. Lee, B. J. Lawrie, and H. Miao, Observation of Unconventional Charge Density Wave Without Acoustic Phonon Anomaly in Kagome Superconductors AV_3Sb_5 ($A = Rb, Cs$), Phys. Rev. X **11**, 031050 (2021).

[25] T. Kato, Y. Li, T. Kawakami, M. Liu, K. Nakayama, Z. Wang, A. Moriya, K. Tanaka, T. Takahashi, Y. Yao, and T. Sato, Three-dimensional energy gap and origin of charge-density wave in kagome superconductor KV_3Sb_5, Commun. Mater. **3**, 30 (2022).

[26] Y. Luo, S. Peng, S. M. L. Teicher, L. Huai, Y. Hu, B. R. Ortiz et al., Distinct band reconstructions in kagome superconductor CsV_3Sb_5, arXiv:2106.01248.

[27] M. Kang, S. Fang, J. Yoo, B. R. Ortiz, Y. M. Oey et al., Charge order landscape and competition with superconductivity in kagome metals, Nat. Mater. **22**, 186 (2023).

[28] D. Shoenberg, Magnetic Oscillations in Metals (Cambridge University Press, Cambridge, 2009).

[29] T. Coffey, Z. Bayindir, J. F. DeCarolis, M. Bennett, G. Esper, and C. C. Agosta, Measuring radio frequency properties of materials in pulsed magnetic fields with a tunnel diode oscillator, Rev. Sci. Instrum. **71**, 4600 (2000).

[30] S. G. Gevorgyan and T. Kiss, Highly sensitive open-flat coil magnetometer of the $\lambda(H, T)$ measurements in plate-like high-T_c cuprates, Rev. Sci. Instrum. **71**, 1488 (2000).

[31] L. Drigo, F. Durantel, A. Audouard, and G. Ballon, Tunnel diode oscillator-based measurement of quantum oscillations amplitude in pulsed high magnetic fields: A quantitative field-dependent study, Eur. Phys. J. Appl. Phys. **52**, 10401 (2010).

[32] See Supplemental Material at http://link.aps.org/supplemental/10.1103/PhysRevLett.130.126401 for the crystal growth process, basic characterization including XRD, electrical transport, details of the TDO measurements including background subtraction from the SdH oscillations, mass plots, Dingle plots, Table S1 listing all observed frequencies, construction of the folded Fermi surface, and Landau level fan diagrams.

[33] Y. Ando, Topological insulator, J. Phys. Soc. Jpn. **82**, 102001 (2013).

[34] G. P. Mikitik and Y. V. Sharlai, Manifestation of Berry's Phase in Metal Physics, Phys. Rev. Lett. **82**, 2147 (1999).

[35] K. Shrestha, R. Chapai, B. K. Pokharel, D. Mierstchin, T. Nguyen, X. Zhou, D. Y. Chung, M. G. Kanatzidis, J. F. Mitchell, U. Welp, D. Popovic, D. E. Graf, B. Lorenz, and W. K. Kwok, Nontrivial Fermi surface topology of the kagome superconductor CsV_3Sb_5 probed by de Haas-van Alphen oscillations, Phys. Rev. B **105**, 024508 (2022).

[36] Y. Fu, N. Zhao, Z. Chen, Q. Yin, Z. Tu et al., Quantum Transport Evidence of Topological Band Structures of Kagome Superconductor CsV_3Sb_5, Phys. Rev. Lett. **127**, 207002 (2021).

[37] W. Zhang, L. Wang, C. W. Tsang, X. Liu, J. Xie, W. C. Yu, K. T. Lai, and S. K. Goh, Emergence of large quantum oscillation frequencies in thin flakes of a kagome superconductor CsV_3Sb_5, Phys. Rev. B **106**, 195103 (2022).

[38] Y. Gan, W. Xia, L. Zhang, K. Yang, X. Mi, A. Wang, Y. Chai, Y. Guo, X. Zhou, and M. He, Magneto-Seebeck effect and ambipolar Nernst effect in the CsV_3Sb_5 superconductor, Phys. Rev. B **104**, L180508 (2021).

[39] D. Chen, B. He, M. Yao, Y. Pan, H. Lin, W. Schnelle, Y. Sun, J. Gooth, L. Taillefer, and C. Felser, Anomalous thermoelectric effects and quantum oscillations in the kagome metal CsV_3Sb_5, Phys. Rev. B **105**, L201109 (2022).

[40] N. N. Wang, K. Y. Chen, Q. W. Yin, Y. N. N. Ma, B. Y. Pan et al., Competition between charge-density-wave and superconductivity in the kagome metal RbV_3Sb_5, Phys. Rev. Res. **3**, 043018 (2021).

[41] M. I. Kaganov and A. A. Slutskin, Coherent magnetic breakdown, Phys. Rep. **98**, 189 (1983).

[42] M. Kartsovnik, High magnetic fields: A tool for studying electronic properties of layered organic metals, Chem. Rev. **104**, 5737 (2004).

[43] N. Harrison, J. Caulfield, J. Singleton, P. H. P. Reinders, F. Herlach, W. Hayes, M. Kurmoo, and P. Day, Magnetic breakdown and quantum interference in the quasi-two-dimensional superconductor in high magnetic fields, J. Phys. Condens. Matter **8**, 5415 (1996).

[44] D. Vignolles, A. Audouard, L. Brossard, S. Pesotskii, R. Lyubovskii, M. Nardone, E. Haanappel, and R. Lyubovskaya, Magnetic oscillations in the 2D network of compensated coupled orbits of the organic metal $(BEDT-TTF)_8$ $Hg_4Cl_{12}(C_6H_5Br)_2$, Eur. Phys. J. B **31**, 53 (2003).

[45] L. M. Falicov and H. Stachowiak, Theory of the de Haas-van Alphen effect in a system of coupled orbits. Application to magnesium, Phys. Rev. **147,** 505 (1966).

[46] A. P. J. van Deursen and J. J. M. Buiting, Magnetic breakdown in incommensurate $Hg_{3-\delta}AsF_6$, J. Phys. F **14,** L101 (1984).

[47] C. Proust, A. Audouard, L. Brossard, S. Pesotskii, R. Lyubovskii, and R. Lyubovskaya, Competing types of quantum oscillations in the two-dimensional organic conductor $(BEDT-TTF)_8Hg4Cl_{12}(C_6H_5Cl)_2$, Phys. Rev. B **65,** 155106 (2002).

[48] N. Harrison, R. G. Goodrich, J. J. Vuillemin, Z. Fisk, and D. G. Rickel, Quantum Interference in LaB_6, Phys. Rev. Lett. **80,** 4498 (1998).

[49] A. B. Pippard, *Magnetoresistance in Metals* (Cambridge University Press, Cambridge, England, 1989).

[50] C. Broyles, D. Graf, H. Yang, X. Dong, H. Gao, and S. Ran, Effect of the Interlayer Ordering on the Fermi Surface of Kagome Superconductor CsV_3Sb_5 Revealed by Quantum Oscillations, Phys. Rev. Lett. **129,** 157001 (2022).

[51] R. Chapai, D. A. Browne, D. E. Graf, J. F. DiTusa, and R. Jin, Quantum oscillations with angular dependence in $PdTe_2$ single crystals, J. Phys. Condens. Matter **33,** 035601 (2021).

[52] C. Li, C. M. Wang, B. Wan, X. Wan, H.-Z. Lu, and X. C. Xie, Rules for Phase Shifts of Quantum Oscillations in Topological Nodal-Line Semimetals, Phys. Rev. Lett. **120,** 146602 (2018).

[53] M. V. Berry, Quantal phase factors accompanying adiabatic changes, Proc. R. Soc. A **392,** 45 (1984).

[54] R. Lou, A. Fedorov, Q. Yin, A. Kuibarov, Z. Tu, C. Gong, E. F. Schwier, B. Büchner, H. Lei, and S. Borisenko, Charge-Density-Wave-Induced Peak-Dip-Hump Structure and the Multiband Superconductivity in a Kagome Superconductor CsV_3Sb_5, Phys. Rev. Lett. **128,** 036402 (2022).

[55] Y. Hu, X. Wu, B. R. Ortiz, S. Ju, X. Han *et al.*, Rich nature of Van Hove singularities in Kagome superconductor CsV_3Sb_5, Nat. Commun. **13,** 2220 (2022).